Journal of The Electrochemical Society, **151** (9) A1489-A1498 (2004)
0013-4651/2004/151(9)/A1489/10/$7.00 © The Electrochemical Society, Inc.

Particle Compression and Conductivity in Li-Ion Anodes with Graphite Additives

C.-W. Wang,[a] Y.-B. Yi,[a] A. M. Sastry,[a,b,*,z] J. Shim,[c,*] and K. A. Striebel[c,*]

[a]*Department of Mechanical Engineering and* [b]*Department of Biomedical Engineering, University of Michigan, Ann Arbor, Michigan 48109-2125, USA*
[c]*Lawrence Berkeley National Laboratory, Environmental Energy Technologies Division, Berkeley, California 94720, USA*

We performed coupled theoretical/experimental studies on Li-ion cells to quantify reductions in anode resistivity and/or contact resistance between the matrix and the current collector with the addition of amorphous carbon coatings and anode compression. We also aimed to identify microstructural changes in constituent particles due to anode compression, using models of permeable-impermeable coatings of graphite particles. We studied three anode materials, SL-20, GDR-6 (6 wt % amorphous carbon coating), and GDR-14 (14 wt % amorphous carbon coating). Four compression conditions (0, 100, 200, and 300 kg/cm^2) were examined. Experimental results indicated that electrical resistivities for unpressed materials were reduced with addition of amorphous carbon coating (for unpressed materials: $\rho_{SL\text{-}20} > \rho_{GDR\text{-}6} > \rho_{GDR\text{-}14}$). Contact resistances were reduced for SL-20 anodes by the application of pressure. Overall, the two-dimensional (2D) impermeable particle mathematical model provided reasonable agreement with the experiments for SL-20 and GDR-6 materials, indicating that coatings remain intact for these materials even at moderate pressures (100 and 200 kg/cm^2). Conductivities of SL-20 and GDR-6 anodes exposed to the highest pressure (300 kg/cm^2) fell short of model predictions, suggesting particle breakage. For the GDR-14 graphite, both 2D models underestimated conductivity for all processing conditions. We conclude that the 2D simulation approach is useful in determining the state of coating.
© 2004 The Electrochemical Society. [DOI: 10.1149/1.1783909] All rights reserved.

Manuscript received August 6, 2003. Available electronically August 18, 2004.

The use of lithium metal, a powerful reducing element, with a strong oxidant (*e.g.*, V_2O_5, MnO_2, $LiNiO_2$, or $LiCoO_2$), allows the realization of high voltage, high energy density cells. But safety and cycle life problems due to the dendritic morphology of the charge-deposited lithium metal have restricted the use of Li as a composite matrix. Recent research has thus focused on improving energy density and cycle life of lithium-ion cells by using graphite, carbon-coated graphite, tin oxide, and intermetallic compounds as Li intercalative host materials.[1-3]

Specifically, high electronic conductivity is critically important in Li intercalative host materials.[4-6] But the high electrical resistivity of graphite matrix materials relative to Li metal in the anode necessitates the use of additives to improve conductivity. Recently, our group has studied improvement of conductivity through the addition of conductive particles.[7] This approach was guided by classical work on effective and percolative properties of systems of high aspect ratio particles.[8-11] Specifically, we have demonstrated that moderate increases in the particle aspect ratio (particle length/particle diameter, L/d) for low-density materials provide significant improvements in electrical conductivity,[7] due to the dramatic reduction in the percolation point.[12]

The use of percolation models allows the prediction of both thermal and electrical conductivity *vs.* density and particle shape. High thermal conductivities of both anodes and cathodes have been shown to be important in preventing thermal runaway, when cells are operated at high temperature. Recently, Maleki and co-workers[13] studied the thermal conductivity of anodes comprised of synthetic graphites of various particle sizes, various fractions of polyvinylidene difluoride (PVDF) binder, and carbon black. Several levels of compression were also used. They found that the highest thermal conductivity was achieved using the largest graphite particles (75 μm), the lowest carbon black content (5%), and the highest pressure (566 kg/cm^2). They also observed a doubling of thermal conductivity at room temperature (27°C) with an increase of pressure from 250 to 575 kg/cm^2. Their results are generally consistent with the percolation model predictions; higher conductivity can be achieved with higher volume fractions of particles, produced by compression of the electrode.

However, high compressive loads can induce high local mechanical loads in active material particles, and ultimately be detrimental to cell performance. For example, Gnanaraj and co-workers[14] studied the effect of compression of anodes (comprised of KS-6 graphite and 10 wt % PVDF binder) and $LiCoO_2$ cathodes, using voltammetry, electrochemical impedance spectroscopy (EIS), and *ex situ* atomic force microscopy (AFM). Electrodes were compressed at 5000 kg/cm^2, using a rolling machine or hydraulic press. The specific capacities were obtained from studies of cyclic voltammograms, in the order of highest to lowest, in unpressed, hydraulically pressed, and rolled electrodes. Higher ac impedance was associated with low kinetic response. Reduced interparticle distance may inhibit Li-ion diffusion among particles and electrolyte and lead to higher ac impedance. Thus, the efforts of Maleki *et al.*[13] and Gnanaraj *et al.*[14] suggest that there may be optimal levels of compression, balancing conductive and mechanical properties.

The structure of carbon matrices in the anode also strongly affects electrochemical performance.[4] Both highly disordered hard carbons and highly ordered graphitized carbons have been shown to produce high capacity. But they both suffer some degree of irreversible capacity loss (ICL), which is putatively related to the surface structure of carbonaceous materials and electrolyte systems. The most commonly used high-permittivity electrolyte solvents include propylene carbonate (PC) and ethylene carbonate (EC). Each has inherent difficulties. EC-based electrolytes are believed to inhibit exfoliation in Li-ion cells with well-crystallized graphitic anodes; however, this phenomenon has not been observed for all types of graphite.[4] One well-known disadvantage of EC electrolytes is that they cannot be used at operating temperatures below −20°C, due to their relatively high freezing point (38°C)[15,16] and rapid dropoff in ionic conductivity at low temperatures.[16]

Ternary or even quanternary mixtures of solvents, such as mixture of EC, dimethyl carbonate (DMC), and PC systems, are commonly used to circumvent these problems.[15,16] However, decomposition of PC-based electrolytes on graphitic surfaces poses a major impediment to their usage. PC reduction produces severe gas formation, creating high, localized particle surface pressures. Solvent percolation in the resulting particle surfaces results in insulation of large portions of the active mass.[17] Thus, suppression of decomposition of PC-based electrolytes is highly desirable. Recently, core-shell types of graphite[18-20] have been used to exploit the turbostratic structure of the carbon coating as illustrated in Fig. 1 to reduce PC cointercalation of Li-ion, and to reduce ICL.

* Electrochemical Society Active Member.
[z] E-mail: sastry@umich.edu

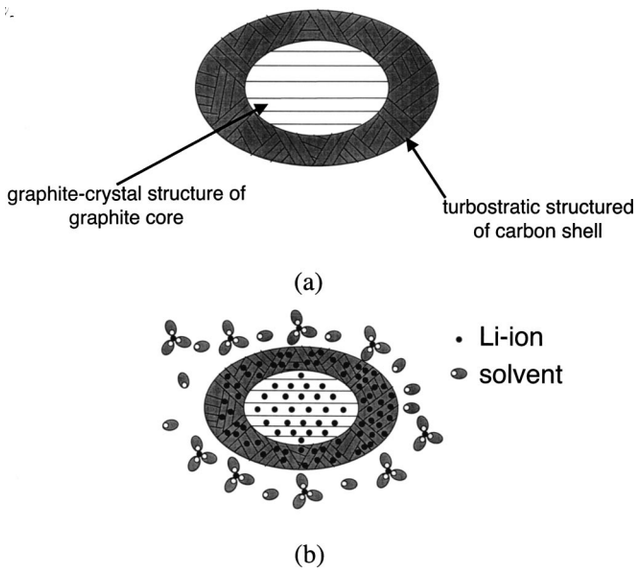

Figure 1. (a) Schematic of core-shell structured graphite and (b) inhibition of electrolyte intercalation into graphene layers.

Uniformity of coating is another key parameter affecting both conductivity and electrochemical performance. Wang and Yoshio and Tsumura and co-workers[19,21] used charge-discharge curves of natural graphite, and carbon-coated graphite anodes in a PC-DMC-based electrolyte to identify possible coating imperfections induced by electrode pressing. They determined that anodes processed at high pressure exhibited the behavior of natural graphite, with a plateau at 0.7 V due to decomposition of the PC. By contrast processing at low pressure resulted in plateaux near 0.2 V.

These workers assumed that coatings (amorphous carbon and/or binder) were uniformly distributed on core particles of natural graphite (Fig. 2a). However, imperfect coatings (Fig. 2b) would be expected to alter the percolation onset, and thus conductivity. Moreover, exposure of the graphite due to coating imperfections would allow electrolyte cointercalation with the Li ion, potentially allowing graphite exfoliation and increased ICL. Also, contact resistance at the particle interfaces would be enhanced for uncoated particles.

Clearly, both material selection and reduction in porosity of anodes are important in assuring good electrochemical performance.

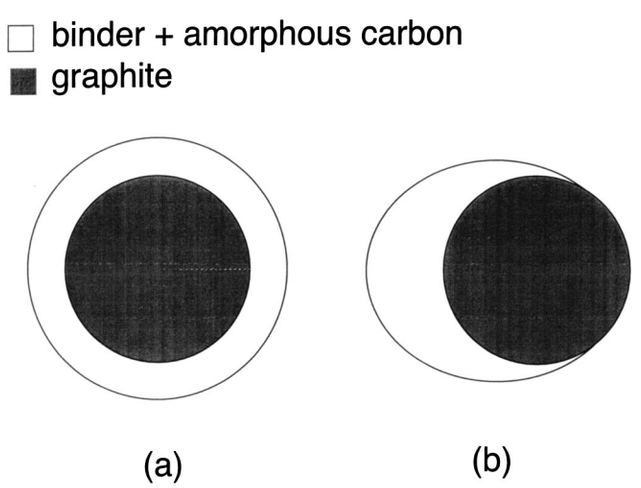

Figure 2. Schematic of possible coating scenarios, including (a) even and (b) uneven coating of binder and amorphous carbon on core particles.

Also, the structure of conductive particles and their permeability relative to one another determine their mechanical and conductive properties, which in turn affect electrochemical performance. The mechanical properties of coated particles, for example, determine whether the outer layers break or deform when particles are forced into close contact. Interparticle permeability (Fig. 2) also strongly affects percolation onset, and thus conductivity.

In the present paper, we investigate the effect of particle coating, permeability, shape and arrangement on experimental and simulated systems of conductive carbon additives. Our objectives were fourfold: (*i*) quantify reductions in anode resistivity and/or contact resistance between matrix and current collector, with the addition of amorphous carbon coatings to conductive carbons used in anodes; (*ii*) quantify reductions in anode resistivity and/or contact resistance with anode compression; (*iii*) identify microstructural changes in constituent particles due to anode compression; and (*iv*) correlate electrical conductivity in real and simulated materials, using permeable coating and impermeable particle models of anodes, to determine the likely connectivity of coated carbon-infused matrix materials.

We also computed standard deviations for all parameters measured, because variability of behavior is a useful parameter in inferring material construction; high variability in resistivity, for example, suggests localized particle agglomeration or damage.

We studied anodes comprised of three different types of natural graphite, pressed to a range of anode densities. These included purified natural graphite from Superior Graphite (SL-20), and two other natural graphites from Mitsui Mining, having 6 wt % (GDR-6) and 14 wt % (GDR-14) coatings of amorphous carbon as described in Ref. 19. Thus, three distinct amorphous fractions were studied. We also conducted a parallel computational study of anode resistivity, involving two-dimensional stochastic models of transport in random arrays of particles. Geometric parameters for these simulations were obtained using image analyses of the materials studied. Electrochemical performance, including voltage profile, ICL, and cyclability of the three types of graphite is discussed in a companion paper.[22]

Approach

Experimental.—Anode preparation and imaging.—Anodes were produced by mixing natural graphite powders with 10 wt % PVDF binder in an *N*-methyl pyrrolidinone (NMP) slurry, and then casting the mixture onto 25 μm Cu foil. Loadings of 2–11 mg active material/cm^2 were used. Anodes were dried under vacuum at 120°C for 12 h and compressed using a benchtop press with smooth plates, at pressures of 100, 200, or 300 kg/cm^2.

Images of the anode were taken using Hitachi S3200N scanning electron microscope (SEM). Sixteen different images at various magnifications ranging from 200 to 1000 times for each graphite with different pressing pressures of 0, 100, 200, or 300 kg/cm^2 were taken at eight locations, including both transverse and horizontal planes of each specimen as indicated in Fig. 3. The SEM images of Fig. 4 illustrate the effect of the application of pressure during electrode preparation on electrode's morphologies at the transverse section and horizontal plane. Image analysis software (NIH Image,[23]) was used to obtain particle center points, orientations, and sizes in each image. These data were later used in simulations. Most particles imaged were approximately elliptical, and thus both major and minor axis lengths were recorded for each particle during image analysis.

Measurement of electrical conductivity.—A four-point probe technique, with method and data reduction discussed previously,[7] was used to determine both top-layer resistivities and contact resistances (between matrix and current collector) in the anodes. Briefly, specimens were placed on a flat, insulating Plexiglas stage, and a Digatron BTS-600 charge-discharge unit was used to supply a small current to an outer probe. The current exited the opposite outer probe, and voltage differences between the second and third (inner)

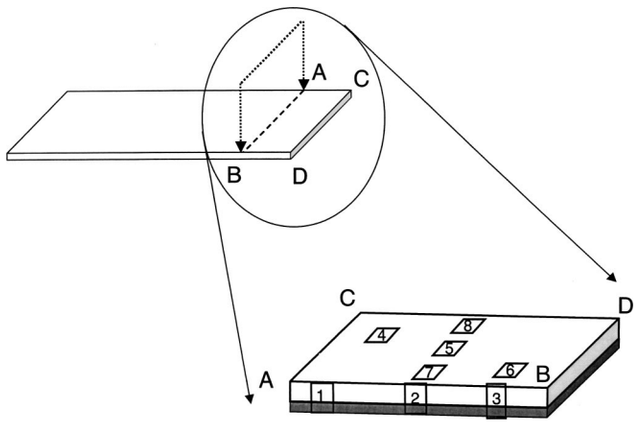

Figure 3. Schematic of the eight locations on specimens where SEM images were taken. At each location, two images with different magnifications were used. Magnifications of 200–300 times were used at locations 1–3; magnifications of 500–1000 times were used at locations 4–8.

probes were measured using an HP-34401 multimeter. This process was repeated for different probe spacings (1.4 and 2.8 mm). The two voltage readings were used to calculate the contact resistance and matrix resistivity by assuming the matrix resistivity was uniform. Depending on the size of the specimen, two or three sets of paired data were taken for each specimen, at different locations. Limitations suggested by Schroder[24] were followed, in which the ratio of sample width to probe spacing was kept larger than 20, and the edge probes (probe 1 or 4) placed a distance at least three times larger than probe spacing from the specimen edge. As previously reported,[7] uncertainties in each measurement were calculated and are reported here.

Theoretical modeling.— Generation of model domains.—Two models for coatings were used in simulations; the permeable coating and the impermeable particle models, shown schematically in Fig. 5. Interparticle contact resistance was ignored, since the binder-coated graphite particles were assumed to have good surface contact (as in Fig. 5a); the effects of departure from this ideal are discussed in a later section.

For the permeable models, systems of particles were generated using statistical codes developed to convert data from image analysis to computational realizations.[7,12,25] Uniform statistical distributions were assumed for particle orientations (0 to 2π radians), and x and y centerpoint locations within the unit cells simulated. Normal distributions were used to define particle aspect ratios (L/D) with means and standard deviations listed in Table I. Thus, for the permeable coating model domains, data from image analysis were used directly, and sizes and locations of overlapping regions were simply outcomes of the centerpoint locations and particle sizes.

The approach for generating arrays was significantly different for impermeable particle simulations, though aspect ratios were again assumed to be normally distributed, with means and standard deviations listed in Table I. Centerpoint locations were determined using dynamic particle collision simulations, in which particles were initially randomly placed, as shown in Fig. 6a. To avoid introducing a scale effect, each ellipse's minor axis length size was kept to less than one-tenth of the unit cell size. Particles were assigned identical initial linear velocities (1/s) and angular velocities (20 rad/s), but randomized directions, as summarized in Table II. At each time step (0.001 s), linear and angular velocities were recalculated, based on collisions among particles, assuming fully elastic collisions of perfectly rigid particles; this process is illustrated in Fig. 6a-c. After 2000 time steps, networks were considered to be at steady state. This number of iterations was found to be a practical value from the authors' related work,[10,11,25] assuring that systems of nonintersecting, or impermeable particles would be achieved for all of the systems studied here. The minimum number of iterations required to reach this state depends, of course, upon volume fraction, particle size, and time step; in this work we did not attempt to optimize simulations for the shortest duration, but instead ran each simulation for the same numbers of time steps and iterations.

After generation of an impermeable realization, the particle shell-core geometries were assigned, as illustrated at Fig. 6d. As mentioned previously, only the cores of the particles were used in generating arrays; the fully permeable shells were added after defining the arrays. The sum of the binder and amorphous carbon mass in each case was used to determine the average thickness of the shell layers; for SL-20 anodes, then, coatings were comprised only of binder. Because of the systematic underrepresentation of shell material due to overlap, continuous adjustments were made in coating thicknesses to assure that final volume fractions were identical to the volume fractions present in the real materials. Periodic boundary conditions were then enforced on each realization, and extraneous (*i.e.*, unconnected) particles were removed, based on the direction in which the voltage was to be applied to the unit cell, as shown in Fig. 6e. For each material analyzed, simulations were performed on twenty realizations for each volume fraction examined.

Conductivity modeling, numerical approach.—Ansoft's Maxwell two-dimensional (2D) finite element software was used to analyze the 2D arrays of both permeable and impermeable particle systems. Electrical resistivities of ellipses and void spaces within the unit cell were set to 1 and 0, respectively, given the relatively negligible conductivity of materials other than graphite in the anode.

The experimental results of matrix electrical conductivity were normalized by the effective conductivity of the multiphase material, as derived classically by Maxwell in Ref. 26. Maxwell solved for electrical potential in fields of inclusions (the Laplace equation). Enforcing continuity, potentials, and current on either side of the interfaces of inclusion and matrix are equated. Effective conductivity is then obtained by equating the total potential in a multiphase domain with an equivalent domain having a single conductivity. Effective conductivity σ_e is thus expressed as a function of conductivity of a continuous medium σ_m, and the conductivity σ_{di}, and volume fraction f_i of each additive phase, as

$$\frac{\sigma_e - \sigma_m}{2\sigma_e + \sigma_m} = \sum_i \frac{(\sigma_{d_i} - \sigma_c) f_i}{(2\sigma_{d_i} + \sigma_c)} \quad [1]$$

Each material studied contained, at most, three additive phases, natural graphite with conductivity σ_g, amorphous carbon coating with conductivity σ_{ac}, and PVDF binder with conductivity σ_P. Graphite is assumed to be the continuous phase, and thus $\sigma_m = \sigma_g$ in Eq. 1. Air is considered to be a fourth inclusion phase (of zero conductivity but finite volume fraction) and so Eq. 1 becomes

$$\sigma_e = \frac{[3\sigma_P(2\sigma_{ac} + \sigma_g) f_P + (2\sigma_P + \sigma_g)(2\sigma_{ac} + \sigma_g) f_g + 3\sigma_{ac}(2\sigma_P + \sigma_g) f_{ac}]}{[(2\sigma_P + \sigma_g)(2\sigma_{ac} + \sigma_g)(3 - 2f_g) - 6\sigma_P(2\sigma_{ac} + \sigma_g) f_P - 6\sigma_{ac}(2\sigma_P + \sigma_g) f_{ac}]} \sigma_g \quad [2]$$

Electrical resistivities of the constituents were determined based on composition and processing conditions of the carbons studied here. Because the amorphous carbons used were produced via ther-

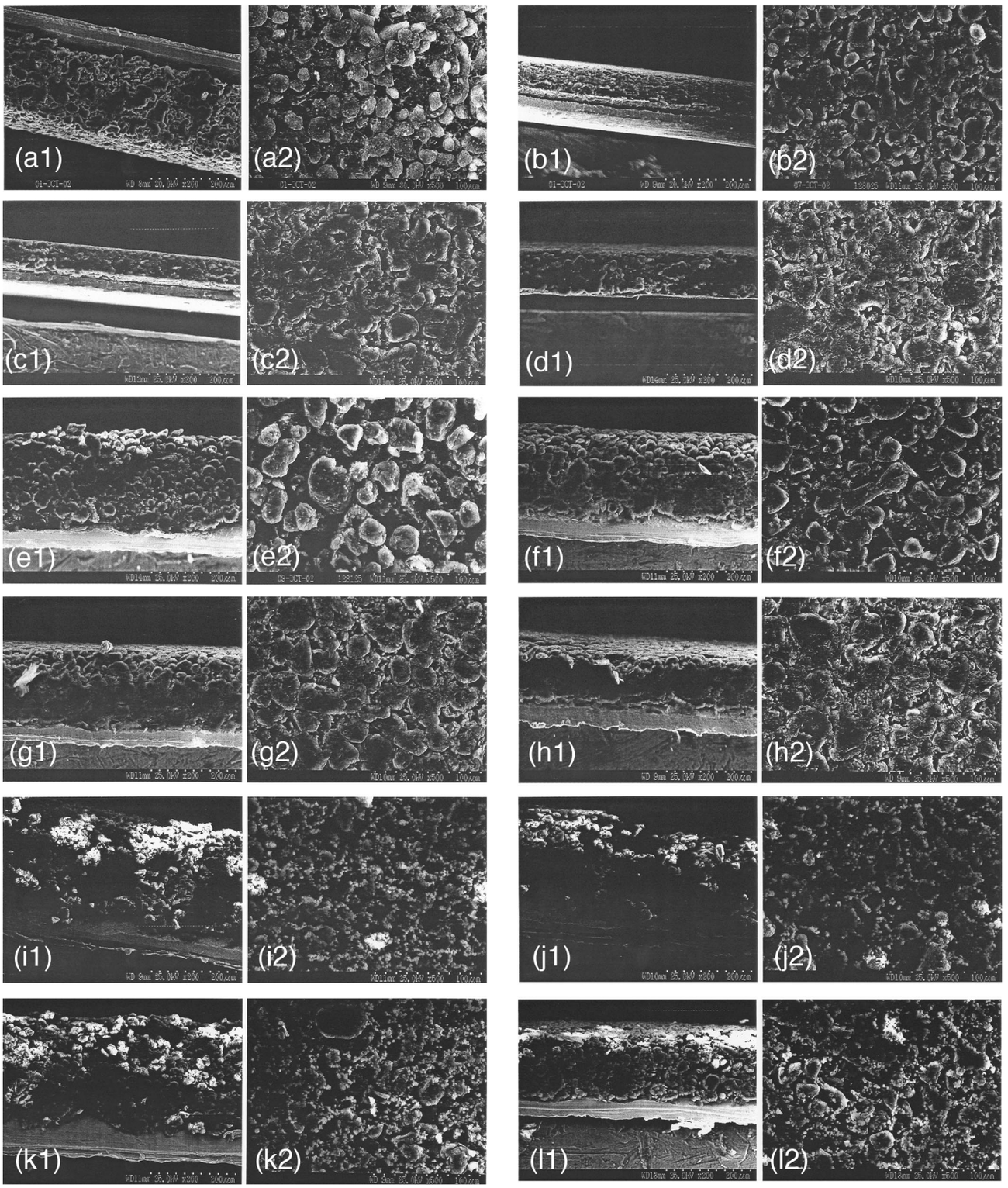

Figure 4. Sequential SEM images of anode particles and interfaces after application of 0, 100, 200 and 300 kg/cm^2 pressure. Images in (a)-(d) are for SL-20 anodes; (e)-(h) are for GDR-6 anodes; (i)-(l) are for GDR-14 anodes.

mal vapor deposition at 1000°C,[18] an empirical approach[27] relating electrical conductivity to processing conditions was used. This expression

$$\sigma = \sigma_0 \exp\left[-\left(\frac{T_0}{T}\right)^{1/4}\right] = 100 \exp\left[-\left(\frac{0.1}{T}\right)^{1/4}\right] \qquad [3]$$

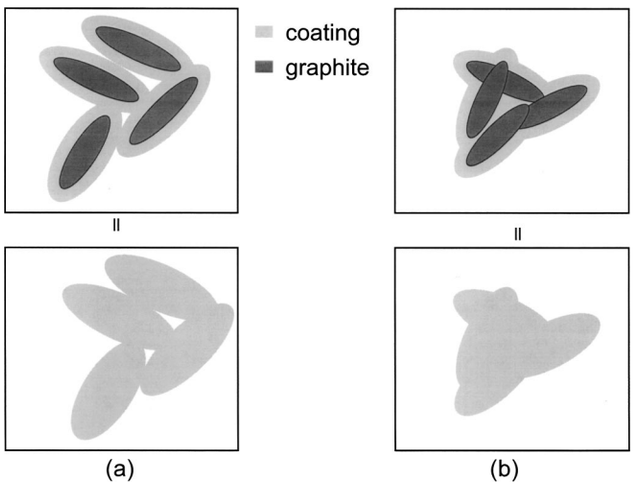

Figure 5. Schematic of (a) the impermeable particle model, wherein only shells are penetrable to one another, and (b) the permeable coating model wherein both cores and shells are penetrable to one another. The lower image in each case was an equivalent domain developed for simulations.

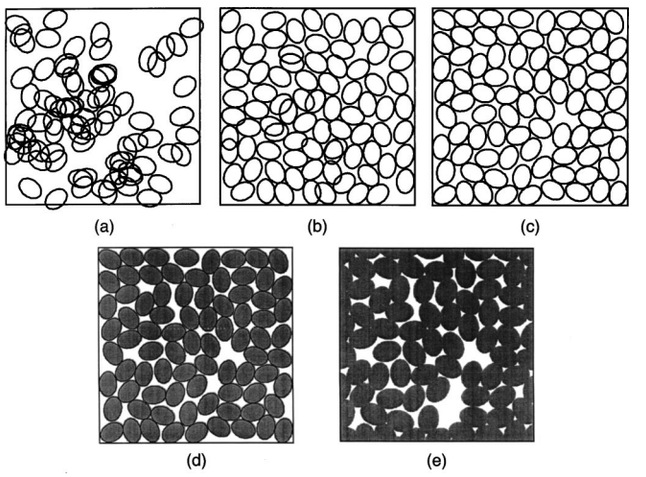

Figure 6. Schematic of the process used in building impermeable model geometries. First, an initial array with overlapping regions was generated (a); after initial particle velocities were initialized, 100 time steps were simulated, resulting in a partially separated system (b); after 2000 time steps, particles were completely separated (c). Then, a shell portion was added to each ellipse (d); finally, periodic boundary conditions were enforced (e). In this example, a reduced volume fraction of 82% was generated.

relates conductivity to two material parameters, σ_0 and T_0, and processing temperature T. Values are 100 ($1/\Omega$ cm), 0.1 ($K^{1/4}$), 300 (K) for σ_0, T_0, and T, respectively, reported for fitting electrical conductivity of anthracene chars in Table V of Ref. 27. For other constituents, such empirical relations were not found, so we selected estimates from the literature; all values are summarized in Table III.[28,29]

Results

Effect of carbon coatings on resistivity/contact resistance.—The roughly equal unpressed porosities in the three materials (~59%) allowed examination of the effect of amorphous carbon additives on resistivity, independent of the effects of pressing. As shown by the data of Table IV, the electrical resistivities for unpressed materials were reduced with additional amorphous carbon coating (for unpressed materials: $\rho_{SL\text{-}20} > \rho_{GDR\text{-}6} > \rho_{GDR\text{-}14}$). The coefficient of variation (standard deviation/average), CV, of graphite matrix electrical resistivity for unpressed materials was approximately 12% for both SL-20 and GDR-6 graphite matrices, but was much larger for the GDR-14 (~78%), indicating that electrical resistivity of graphite matrix was more consistent throughout the specimens for SL-20 and GDR-6.

To investigate the effect of addition of amorphous carbon on contact resistance, unpressed material properties were again compared. As shown in the data of Table IV, average contact resistance, R^c, decreased with additional carbon coating (*i.e.*, $R^c_{SL\text{-}20} > R^c_{GDR\text{-}6} > R^c_{GDR\text{-}14}$). But the CV of contact resistance was significantly higher in the material of highest amorphous carbon weight fraction. We found this value to be roughly 21% for SL-20 and 13% for GDR-6, but approximately 49% for GDR-14.

Effect of anode compression on resistivity/contact resistance.—Figure 7a-c allow comparisons among experimental electrical resistivities, ρ, of unpressed and pressed materials. Densities and conductivities, predictably, increased with higher processing pressure. Variabilities in these measurements decreased significantly with increasing compression for the SL-20 and GDR-6 anodes, but less so for the GDR-14 anodes. The reduction ratios in resistivity for the highest compression ($\rho_{unpressed}/\rho_{300\ kg/cm2}$) were, in order of highest to lowest, SL-20 ($\rho_{unpressed}/\rho_{300\ kg/cm2} = 7.91$), GDR-6 ($\rho_{unpressed}/\rho_{300\ kg/cm2} = 3.92$), and GDR-14 ($\rho_{unpressed}/\rho_{300\ kg/cm2} = 1.41$).

Table I. Mass density, particle sizes and distributions, and porosity for the SL-20, GDR-6, and GDR-14 anodes, before and after compression.

Graphite type	Applied pressure (kg/cm^2)	Active material thickness (mm)	Material density (g/cm^3)	Porosity (%)	Particle length (μm)			Particle diameter (μm)			Aspect ratio
					Average	Standard deviation	Coefficient variation (%)	Average	Standard deviation	Coefficient variation (%)	
SL-20	0	0.154	0.84	59.36	23.23	8.25	35.51	16.64	5.75	34.56	1.41
	100	0.104	1.45	32.65	24.25	7.4	30.52	16.96	4.34	25.59	1.44
	200	0.09	1.73	17.31	22.63	6.05	26.73	16.70	4.43	26.53	1.38
	300	0.084	1.98	9.93	22.43	6.05	26.97	16.07	3.36	20.91	1.40
GDR-6	0	0.125	0.95	55.19	31.47	9.82	31.20	21.83	5.81	26.61	1.46
	100	0.1	1.22	42.35	30.82	8.36	27.13	22.2	5.50	24.77	1.40
	200	0.078	1.44	32.27	31.35	8.42	26.86	23.26	5.84	25.11	1.36
	300	0.08	1.71	19.27	31.22	8.83	26.68	22.84	5.66	24.78	1.38
GDR-14	0	0.116	0.84	59.54	29.46	7.74	26.27	20.82	5.07	24.35	1.43
	100	0.096	1.25	40.20	28.46	7.52	26.42	20.72	5.01	24.18	1.38
	200	0.092	1.38	33.56	27.04	7.81	28.88	19.69	5.82	29.56	1.39
	300	0.087	1.43	31.25	25.00	5.68	22.72	17.46	3.79	21.71	1.46

Table II. Kinetic parameters assigned for ellipses, used in collision simulations for generation of impermeable particle geometries.

Iteration number	Time step (s)	Initial linear velocity (s^{-1})	Initial angular velocity (rad/s)
2000	0.001	1.0	20.0

Table III. Assumed resistivities for constituents of anodes.

Material types	Resistivity ($\mu\Omega$ cm)
Natural graphite	6.00×10^3
Cu foil	1.71
PVDF	1.00×10^{21}

As shown by the data of Table IV, contact resistances were reduced for SL-20 anodes by the application of pressure, but actually increased for both the GDR-6 and GDR-14 anodes. Coefficients of variation for contact resistance fluctuated for SL-20 graphite anodes with increasing pressure, dropping from 20 to 6.6% and then increasing to 17%. Coefficients of variation in the GDR series anodes were somewhat higher, falling between 13 to 54% for GDR-6, and between 16 to 87% for GDR-14.

Effect of compression on particle microstructure.—Matrix mass density increased monotonically with increasing pressure on all electrodes. These densities are reported in Table IV. However, the degrees of change in porosity were different for the anode types. In order of highest to lowest, these were, SL-20 ($\phi_{\text{unpressed}}/\phi_{300\ \text{kg/cm2}} = 5.98$), GDR-6 ($\phi_{\text{unpressed}}/\phi_{300\ \text{kg/cm2}} = 2.86$), GDR-14 ($\phi_{\text{unpressed}}/\phi_{300\ \text{kg/cm2}} = 1.91$), corresponding to increased amorphous carbon content.

Analysis of SEM images (Fig. 4a-l) showed that smaller particle sizes were present in SL-20 than either the GDR-6 or GDR-14 anodes; data from image analysis are reported in Table I. Particle sizes listed at Table I were obtained from top-layer images, as shown in Fig. 3, locations 4–8. As shown in the sample images of Fig. 4, individual particle boundaries in SL-20 and GDR-6 were less distinguishable at low porosity (or after compression) than in GDR-14 anodes at the top surface. Also, a compacted zone developed near the interface of the current collector and graphite matrix, as shown in the transverse plane views of sectioned electrode, in the left images of each subfigure of Fig. 4. This inhomogeneous deformation was more pronounced at higher pressures.

The SL-20 anodes showed the greatest relative thickness change due to pressurization. This can be readily seen by examination of data in Table I and Table IV. Though SL-20 anodes were of initial thicknesses 0.154 mm (as compared with 0.125 and 0.116 mm, for GDR-6 and GDR-14, respectively), at the highest pressure tested, the anodes were of approximately equal thickness (0.08–0.09 mm). Thus, the porosity of the SL-20 anodes at the highest compression was significantly lower than either the GDR-6 or GDR-14 anodes (9.93% *vs.* 19.27% and 31.25%, respectively).

Comparison of simulations and experiments: material connectivity.—Comparisons among simulations and experimental results are presented in Fig. 8. 2D impermeable particle and permeable coating model results are included in each comparison.

Agreement between models and experiments showed similar trends for SL-20 and GDR-6 anodes, as reported in Fig. 8a and b. 2D models underestimated conductivity in unpressed anodes for both materials, but provided good agreement with experimental data for pressed materials. The 2D impermeable particle model provided better agreement than the permeable coating model for both materials. Normalized experimental conductivities of anodes processed at moderate pressures (100 and 200 kg/cm^2) fell between predictions of the two models. Conductivities of SL-20 and GDR-6 anodes exposed to the highest pressure (300 kg/cm^2) fell short of both models' predictions.

For the GDR-14 graphites, both of the 2D models underestimated conductivity for all processing conditions, as shown in Fig. 8c. The best agreements found between simulated and actual conductivities were for the 2D permeable coating model at high pressures.

Discussion

Effect of carbon coatings on resistivity/contact resistance.—Electrical resistivity is closely related to reaction kinetics. As reported, electrical resistivity and contact resistance at the interface of the current collector and graphite matrix improved with increasing carbon coating content for unpressed materials. Use of an amorphous coating, without pressing, improves this important property. The trends in coefficients of variation in these measurements also allow some inference as to distribution of particles. Specifically, the relatively higher CVs in resistivities of the GDR-14, *vs.* the SL-20

Table IV. Measured resistivities and contact resistances for anode materials, for each of the pressures studied.

Graphite type	Applied pressure (kg/cm^2)	Porosity (%)	Resistivity ($\mu\Omega$ cm) Average	Resistivity ($\mu\Omega$ cm) Standard deviation	Resistivity ($\mu\Omega$ cm) Coefficient variation (%)	Contact resistance ($\mu\Omega$ cm^2) Average	Contact resistance ($\mu\Omega$ cm^2) Standard deviation	Contact resistance ($\mu\Omega$ cm^2) Coefficient variation	Uncertainty (%)
SL-20	0	59.36	1.51×10^6	1.87×10^5	12.38	3.59×10^6	7.36×10^5	20.50	15.93
	100	32.65	3.81×10^5	4.32×10^4	11.34	1.54×10^6	1.11×10^5	7.21	16.00
	200	17.31	1.88×10^5	3.41×10^4	18.14	1.50×10^6	9.84×10^4	6.56	16.03
	300	9.93	1.91×10^5	1.78×10^4	9.32	1.10×10^6	1.95×10^5	17.73	16.02
GDR-6	0	55.19	2.64×10^5	3.17×10^4	12.01	1.18×10^4	1.48×10^3	12.54	25.04
	100	42.35	1.62×10^5	3.30×10^4	20.37	1.44×10^4	7.72×10^3	53.61	22.58
	200	32.27	6.39×10^4	1.91×10^4	29.89	2.22×10^4	2.16×10^2	0.97	15.43
	300	19.27	6.73×10^4	3.20×10^4	47.55	3.29×10^4	7.91×10^3	24.04	15.62
GDR-14	0	59.54	3.95×10^4	3.09×10^4	78.23	2.96×10^3	1.46×10^3	49.32	16.47
	100	40.20	1.71×10^4	7.01×10^3	40.99	2.91×10^3	1.88×10^3	64.60	15.11
	200	33.56	3.50×10^4	2.19×10^4	62.57	3.52×10^3	3.06×10^3	86.93	15.38
	300	31.25	2.81×10^4	1.62×10^4	57.65	5.40×10^3	8.68×10^2	16.07	19.43

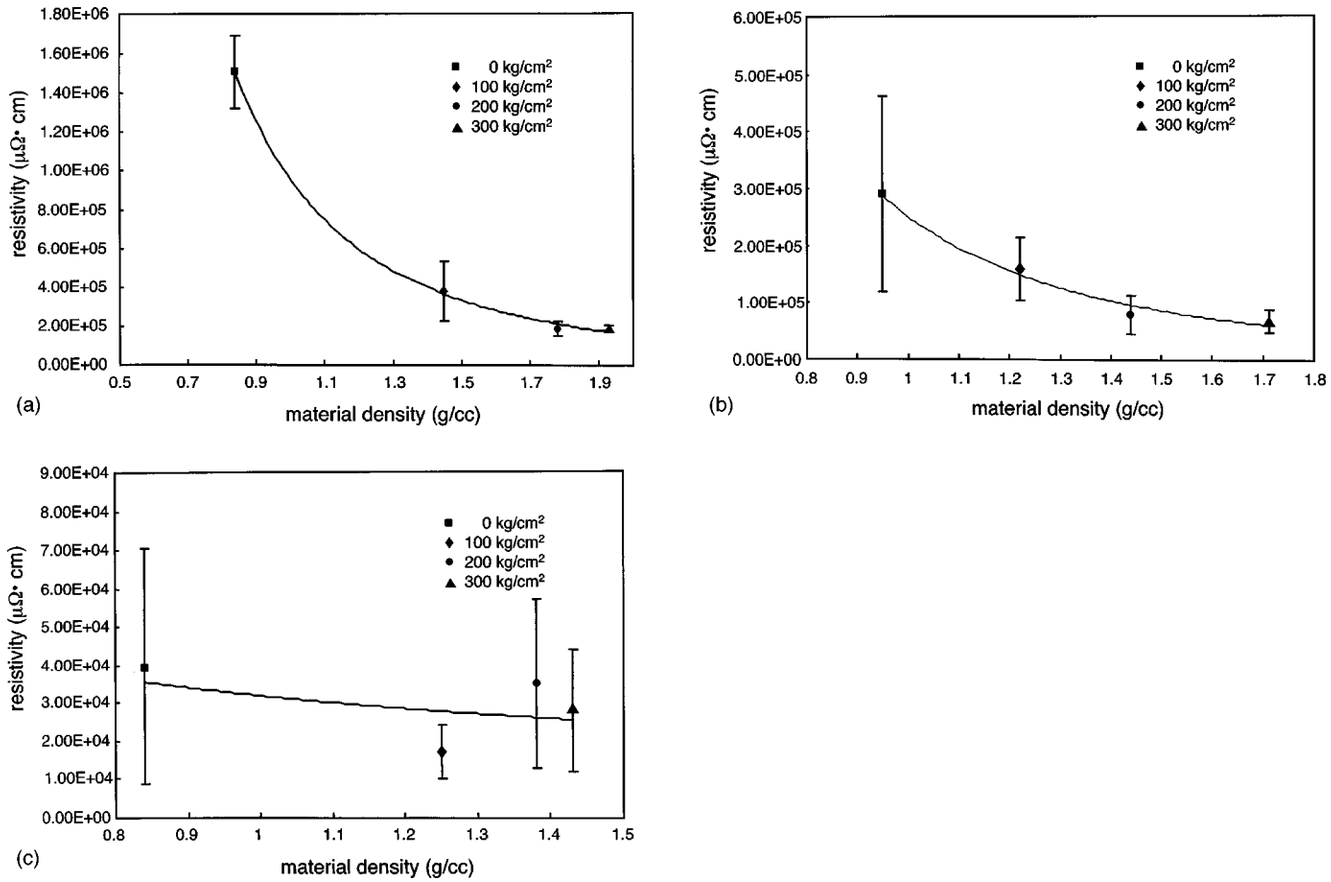

Figure 7. Experimental results of electrical resistivity *vs.* material densities, for (a) SL-20, (b) GDR-6, and (c) GDR-14 anodes.

and GDR-6 anodes, suggest that these latter two types had a more uniform distribution of conductive mass, or that coatings in the GDR-14 electrode themselves were nonuniform. This last possibility is discussed in later sections.

Effect of anode compression on resistivity/contact resistance.—Contact resistance at the interface can serve as an indication of state of contact between particles and the current collector, since contact resistance is inversely proportional to the contact area. As per material compositions listed in Table I, the constituent particles of SL-20 anodes were found to be much smaller than those in the GDR series anodes. Comparison of data in Tables I and IV confirms that the SL-20 anodes did exhibit the lowest contact resistance. Only the SL-20 anodes showed reduction in contact resistance with increasing pressure, though all materials showed reductions in overall matrix resistivity.

The higher CV in measured resistivity in pressed and unpressed GDR-14 anodes is consistent with particle damage or agglomeration at particles near the interface, though this effect was not observed in the lower weight-fraction amorphous carbon-coated material (GDR-6). In both of the other anode types (SL-20 and GDR-6), CV in measured resistivities dropped with increasing pressure (Fig. 7a and b). This would be expected based on prior simulations and analysis: at higher volume fractions systems of identical particles exhibit lower, more deterministic percolation thresholds.[25] These lower percolation thresholds result in higher conductivities, with lower variances. Thus, the high variability observed in the GDR-14 anodes may reflect a criticality in coating vis-à-vis mechanical stress. Excessively thick coatings may be more susceptible to damage in general (as seen by resistivity measurements) and at interfaces in particular (as seen by contact resistance measurements). Breakdown of the coatings under mechanical load, especially at the interface between matrix and current collector, merits further attention.

Effect of compression on particle microstructure.—As shown in the sample SEM images of Fig. 4 and the data of Table I, compression did affect particle structure, especially in the transverse direction. In all cases, particles became preferentially compacted near the current collector interface; this effect was more pronounced with increasing pressure.

Particle cracking and exposure of graphite cores to solvents must be avoided in pressurization of coated anodes. As mentioned earlier, optimality in coating design requires the determination of critical loads that produce such cracking. Thus, the nonuniformity of compaction merits further study, especially since it appeared to be more pronounced in the coated, GDR electrodes.

The higher relative densities produced in compressed SL-20 anodes, relative to the other anode types, implies that particles were polydisperse and/or aligning in the plane of the anode. Image analysis data do not support the former hypothesis: CVs in both particle diameters and lengths decreased with increasing pressure in the SL-20 anodes, and neither average dimension changed significantly. To investigate the latter hypothesis, on realignment of particles, we compare the densities of electrodes with the theoretically maximum densities of the systems at the highest pressure.

It is well known (see representative volume element of Fig. 9a) that the packing limit for monodisperse spheres [for either hexagonal close-packed (hcp) or face-centered cubic (fcc) packed planes] is 74% in terms of volume fraction. For regular arrays of ellipsoids with aligned axes, Fig. 9b, we can derive the maximum packing fraction as follows. Beginning with an fcc unit cell containing four

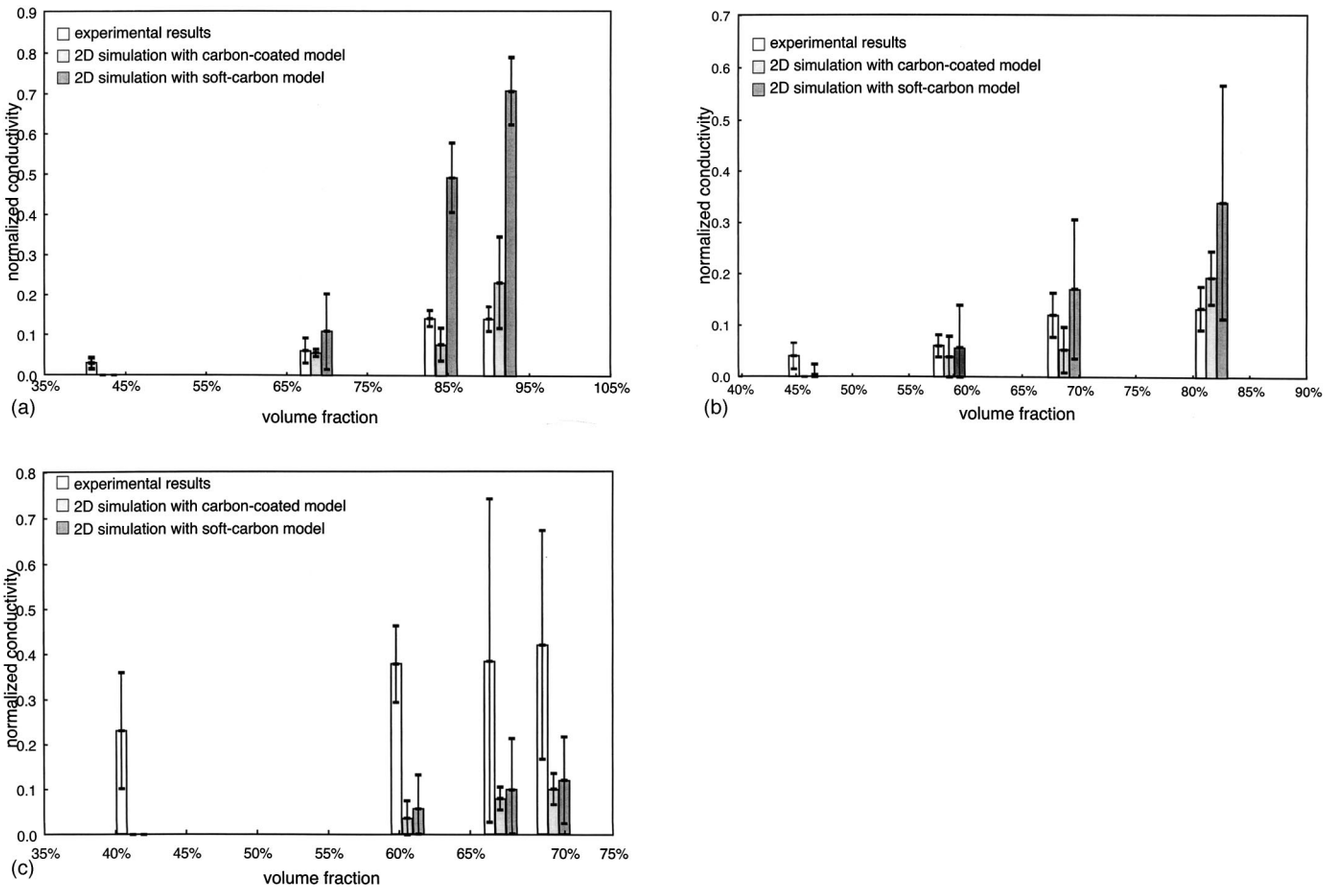

Figure 8. Comparisons between normalized experimental data and theoretical predications assuming 2D impermeable particles and permeable coating models for (a) SL-20, (b) GDR-6, and (c) GDR-14 anodes.

spheres, we have immediately the inclusion volume $(16/3)\pi R^3$, where R is the radius of the sphere. The length of the cell side is $4R/\sqrt{2}$, and therefore the cell volume is $32R^3/\sqrt{2}$. The volume fraction is thus a ratio of these two values, namely, $\sqrt{2}\pi/6 \approx 74.05\%$.

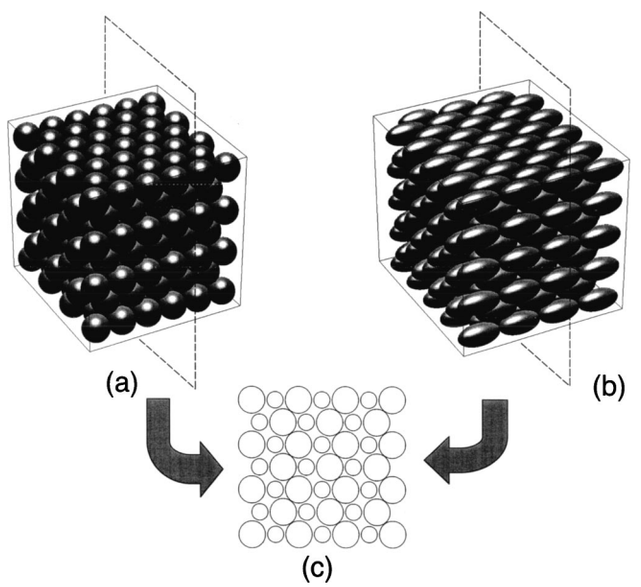

Figure 9. Close packing configurations for (a) spheres and (b) axially aligned ellipsoids. (c) Common cross-sectional profile for both (a) and (b).

If we elongate the cell and all interior spheres by a factor of a, b, and c along the three axes of the coordinate system, the total volume of the ellipsoids becomes $(16/3)\pi abc$, and the cell volume is $32abc/\sqrt{2}$, resulting in an identical volume fraction as for the fcc packed spheres. Thus, the maximum packing fraction for monodisperse, axially aligned ellipsoids is identical to the hcp or fcc limit for spheres. We further note that the maximum packing fractions of arrays of both spheres and ellipsoids has been studied (*e.g.*, Ref. 30), but that all of these fractions contain some assumptions as to particle interaction, which have not yet been determined for these graphite systems. Thus, we compare particle densities to the ideal case as a benchmark.

Clearly, the densities achieved via the highest pressures used here do not exceed the theoretical limit for axially aligned particles, even though our systems were polydispersed. We would expect to see somewhat higher limits for maximum packing fractions for systems containing wider distributions of size. Thus, there is little basis for assuming that particles were fractured at any of the volume fractions studied, based only on densities. Further examination of particle deformation must be studied using alternative types of image analysis and more detailed mechanical modeling of the systems.

Comparison of simulations and experiments: material connectivity.—For unpressed, high porosity anodes, simulations severely underpredicted conductivity. The percolation threshold for particles of aspect ratio 1.4[10,11] is ~66% (*i.e.*, 34% porosity) for 2D model

but is ~28% (*i.e.*, 72% porosity) for 3D model, just below the unpressed porosities of the three materials studied. Most of the computational realizations thus resulted in unpercolated systems at high porosity, and thus zero-conductivity domains. This is a weakness in the use of such models for porous materials, rather than composites having matrices of finite conductivity. Simulations of systems of particles having a porosity or density near the percolation point display highly probabilistic transport properties, since finite transport properties require percolation. However, real processes assure that such systems are percolated, since unpercolated systems simply do not form matrices; sufficient mass in physical systems is simply a first requirement in materials manufacture.

At moderate pressures (100–200 kg/cm^2), simulated conductivities for the two models used bounded experimental conductivities for SL-20 and GDR-6 anodes. The state of coating (whether permeable or impermeable), however, did not strongly affect predicted conductivities with the amorphous carbon-coated materials. Only in the binder-only material, the SL-20, did these predictions differ significantly (compare two models' predictions for conductivity in Fig. 8a *vs.* Fig. 8b and c). Specifically, at the highest pressure (*i.e.*, highest material density) examined for the SL-20 anodes, fully permeable coatings produced an approximately threefold improvement in predicted conductivity over impermeable coatings (Fig. 8a, 90% volume fraction). This is a result of the high resistivity of binder relative to that of amorphous carbon; mixtures of amorphous carbon and binder are much closer in conductivity to natural graphite, and so the state of coating permeability has less effect on material resistivity, in general. Furthermore, high permeability of coatings also results in higher densities at the same pressures, in general. These findings support the selection of binder materials and processing conditions which produce permeable coatings on graphite, both for mechanical stability and for high conductivity.

As mentioned earlier for the GDR-14 anodes, both of the 2D models severely underestimated conductivity, at all pressures, as shown in Fig. 8c. This lack of agreement has several possible sources. First, the inhomogeneous compaction of the material, shown in Fig. 4j-k, may have required that 3D simulations be used, which could lead to errors in reduction of experimental data. Second, the application of pressure may have altered the particle size distributions throughout the anodes. Distributions reported here were only for surface particles (limited by SEM capability). Distributions of particle sizes throughout the specimen would be required to determine whether or not particle breakage occurred. Still, the high conductivities suggest rearrangement of amorphous carbons to produce highly conductive regions closer to the current collector. The study of graded properties in highly compacted anodes is merited if these prove electrochemically attractive.

Dimensionality in simulation.—Our previous simulations showed that 2D models were applicable to systems of particles wherein the ratio of specimen thickness to particle size falls within 1 to 5.[25] This ratio for the materials studied here ranged from 5.23–9.25 for SL-20, 3.35–5.73 for GDR-6, and 4.98–5.57 for GDR-14, for pressures of 300 kg/cm^2, and zero, respectively. Thus, use of a 2D model for compressed materials is reasonable, especially for the GDR-6 and GDR-14. However, a 3D model may be much more suitable for SL-20 materials. The closeness of the volume fraction of GDR-14 processed at 300 kg/cm^2 to the 2D percolation threshold is ~66% volume fraction, assures underprediction of model results to experiments, which must be considered.

The collision model used in generating 2D systems of polydisperse, impermeable particles was much simpler than would be required in generating 3D systems. Although some effort has been dedicated to modeling maximum packing fractions in random, 3D materials,[30] the maximum packing density for polydisperse spheres or circles is still unknown. Examination of 3D systems may be required for thicker anodes (*i.e.*, high energy rather than high power systems), but development of packing algorithms for these will be nontrivial.

Conclusions

Overall, as shown by the data of Table IV, for the conditions studied, application of pressure to anodes was less effective than the addition of carbon coating in improving anode electrical conductivity. Improvements in electrical conductivities from unpressed values of factors of 8, 4, and 1.4, respectively SL-20, GDR-6, and GDR-14 were observed at the highest compressions. However, factors of improvement of 5.7 and 38 were obtained with addition of 6 and 14% carbon coating.

Additionally, application of high pressure has the potential to induce particle damage, as supported here by high observed CVs for contact resistance. Greater exposure of graphite in fractured particles is a major concern, and so determination of optimal pressures is critical and merits further study.

The simulations presented here provided a systematic way to investigate the state of coating of particles. For the three natural graphite-based materials studied here, the experimental data after compression was within the predictions of 2D impermeable and 2D permeable model, except for GDR-14 electrodes, which is consistent with the disruption of coating. Further electrochemical testing of these systems will help determine the coating state.

Adding capability to model contact resistance among particles will be required to improve the understanding of the state of coating. 3D models will also be investigated, based on the thicknesses of interest in anodes. Recently, we have developed analytic approximations, in the form of integral expressions and series expansions, of percolation points in monodisperse 2D[10] and 3D[11] systems; these will form a basis for determining transport properties of multiphase, polydisperse systems.

Acknowledgments

This work was generously supported by the Department of Energy BATT Program, and the Synthetic Multifunctional Materials Program of DARPA (Dr. Leo Christodoulou, Program Director, DARPA; Dr. Steve Fishman, Program Director, ONR). Additional support was provided by an NSF PECASE Award (A.M.S.). Materials and technical advice were provided by the Lawrence Berkeley Laboratories (Dr. Frank McClarnon), and the Institut de Recherche d'Hydro-Quebec (Dr. Karim Zaghib). We gratefully acknowledge these sponsors and colleagues.

University of Michigan assisted in meeting the publication costs of this article.

List of Symbols

A	area
CV	coefficient of variation (standard deviation/mean)
D	particle diameter in minor axis direction
f_i	volume fraction of *i*th phase
G	electrical conductance
L	particle diameter in major axis direction
R^c	contact resistance at the interface of matrix and current collector
T	working environment temperature
T_0	heat-treatment temperature
Z	ac impedance
ϕ	porosity
ρ_i	electrical resistivity of *i*th (SL-20, GDR-6, or GDR-14) type of compression condition
σ_{ac}	electrical conductivity of amorphous carbon phase
σ_{di}	electrical conductivity of *i*th inclusion phase material
σ_e	effective conductivity of multiphase material
σ_m	conductivity of matrix-phase medium
σ_p	electrical conductivity of PVDF phase
σ_g	electrical conductivity of graphite phase

References

1. A. Herold, *Bull. Soc. Chim. Fr.*, **7-8**, 999 (1955).
2. I. A. Courtney and J. R. Dahn, *J. Electrochem. Soc.*, **144**, 2045 (1997).
3. K. D. Kepler, J. T. Vaughey, and M. M. Thackeray, *Electrochem. Solid-State Lett.*, **2**, 307 (1999).
4. S. Flandrois and B. Simon, *Carbon*, **37**, 165 (1999).
5. J. B. Goodenough, in *Lithium Ion Batteries—Fundamentals and Performance*, M. Wakihara and O. Yamamoto, Editors, p. 1, Wiley-VCH, New York (1998).
6. S. Y. Chung, J. T. Bloking, and Y. M. Chiang, *Nat. Mater.*, **1**, 123 (2002).

7. C. W. Wang, K. A. Cook, and A. M. Sastry, *J. Electrochem. Soc.*, **150**, A385 (2003).
8. Z. Hashin, *Int. J. Solids Struct.*, **21**, 711 (1985).
9. S. Kirkpatrick, *Rev. Mod. Phys.*, **45**, 574 (1973).
10. Y. B. Yi and A. M. Sastry, *Phys. Rev. E*, **66**, 066130 (2002).
11. Y. B. Yi and A. M. Sastry, *Proc. R. Soc. London*, **460**, 2353 (2004).
12. X. Cheng and A. M. Sastry, *Mech. Mater.*, **31**, 765 (1999).
13. H. Maleki, J. R. Selman, R. B. Dinwiddie, and H. Wang, *J. Power Sources*, **94**, 26 (2001).
14. J. S. Gnanaraj, Y. S. Cohen, M. D. Levi, and D. Aurbach, *J. Electroanal. Chem.*, **516**, 89 (2001).
15. C. X. Wang, H. Nakamura, H. Komatsu, M. Yoshio, and H. Yoshitake, *J. Power Sources*, **74**, 142 (1998).
16. M. C. Smart, B. V. Ratnakumar, and S. Surampudi, *J. Electrochem. Soc.*, **146**, 486 (1999).
17. D. Aurbach, B. Markovsky, I. Weissman, E. Levi, and Y. Ein-Eli, *Electrochim. Acta*, **45**, 67 (1999).
18. M. Yoshio, H. Y. Wang, K. Fukuda, Y. Hara, and Y. Adachi, *J. Electrochem. Soc.*, **147**, 1245 (2000).
19. H. Y. Wang and M. Yoshio, *J. Power Sources*, **93**, 123 (2001).
20. T. Tsumura, A. Katanosaka, I. Souma, T. Ono, Y. Aihara, J. Kuratomi, and M. Inagaki, *Solid State Ionics*, **135**, 209 (2000).
21. H. Y. Wang, M. Yoshio, T. Abe, and Z. Ogumi, *J. Electrochem. Soc.*, **149**, A499 (2002).
22. K. A. Striebel, J. Shim, A. Sierra, C. W. Wang, and A. M. Sastry, *J. Power Sources*, Accepted.
23. http://rsb.info.nih.gov/nih-image/ (2001).
24. D. K. Schroder, *Semiconductor Material and Device Characterization*, 2nd ed., John Wiley & Sons, New York (1998).
25. Y. B. Yi, C.-W. Wang, and A. M. Sastry, *J. Electrochem. Soc.*, **151**, A1292 (2004).
26. R. E. Meredith and C. W. Tobias, in *Advances in Electrochemistry and Electrochemical Engineering*, Vol. 2, C. W. Tobias, Editor, p. 15, Interscience, New York (1962).
27. P. Delhaes and F. Carmona, in *Chemistry and Physics of Carbons*, P. L. J. Walker and P. A. Thrower, Editors, Marcel Dekker, Inc., New York (1981).
28. http://www.matweb.com (2003).
29. PVDF resistivity data from Quadrant Engineering Plastic Products and cited from http://www.matweb.com (2003).
30. S. Torquato, *Random Heterogeneous Materials: Microstructure and Macroscopic Properties*, p. 168, Springer, New York (2002).